PCCP

Accepted Manuscript

This is an *Accepted Manuscript*, which has been through the Royal Society of Chemistry peer review process and has been accepted for publication.

Accepted Manuscripts are published online shortly after acceptance, before technical editing, formatting and proof reading. Using this free service, authors can make their results available to the community, in citable form, before we publish the edited article. We will replace this *Accepted Manuscript* with the edited and formatted *Advance Article* as soon as it is available.

You can find more information about *Accepted Manuscripts* in the **Information for Authors**.

Please note that technical editing may introduce minor changes to the text and/or graphics, which may alter content. The journal's standard **Terms & Conditions** and the **Ethical guidelines** still apply. In no event shall the Royal Society of Chemistry be held responsible for any errors or omissions in this *Accepted Manuscript* or any consequences arising from the use of any information it contains.

Multifunctional Biosensors Based on Peptide-Polyelectrolyte Conjugates

S. Kogikoski Jr[a], C. P. Sousa[a], M. S. Liberato[a], T. Andrade-Filho[b], T. Prieto [a], F. F. Ferreira [a], A. R. Rocha[c], S. Guha[d], W. A. Alves [a] *

A novel enzymatic platform for the sensing of H_2O_2 and glucose that uses L,L-diphenylalanine micro/nanostructures (FF-MNSs) as enzyme support is shown. This platform is obtained by the self-assembly of poly(allylamine hydrochloride) (PAH), FF-MNSs, and microperoxidase-11 (MP11) anchored on the peptide matrix, in two different crystal structures of FF-MNSs: hexagonal ($P6_1$) and orthorhombic ($P22_12_1$). The electroactive area of the electrodes increases with the presence of the FF-MNSs. We also demonstrate via Theoretical calculations that the valence band energy of the orthorhombic structure allows it to be doped, similarly to p-type semiconductors, where PAH acts as a doping agent for the orthorhombic peptide structure, decreasing the band-gap in around 1 eV, that result in a smaller charge transfer resistance. These results are consistent with electrochemical impedance spectroscopy measurements, which further elucidates the role of the band structure of the orthorhombic FF-MNSs in the conductivity and electron transfer rates of the hybrid material. An effective communication between the electrode and the active site of a Glucose Oxidase enzyme through MP11-protein complexes occurs, paving the way for FF-MNSs in the orthorhombic phase for future development of bioelectronics sensing devices.

1 Introduction

Ever since the discovery of diphenylalanine (FF) nanotubes by Reches and Gazit,[1] researchers have been exploring their potential in biological and biomedical applications.[2, 3] Particularly, extensive studies of the diphenylalanine nanotubes indicated that they exhibit significant rigidity, mechanical,[4] and thermal stability.[5] Furthermore, these nanotubes have shown to possess intrinsic photoluminescence[6] and piezoelectric functionality,[7] and their utilization for biosensing[8, 9] and light harvesting[10] have been demonstrated. The formation of elongated structures with highly hierarchical order – introduced by the self-assembly process – makes those structures appealing for electronic applications.[11, 12] In addition, it has been suggested that ferrocene-modified phenylalanine monomer aggregates in water via a rapid self-assembly mechanism to form stable hydrogels.[13] The good biocompatibility of the hydrogels maintains the bioactivity of Acetylcholinesterase (AChE), and the large number of ferrocene moieties contained in the hydrogels acts as the redox mediators for AChE.[14] Peptide sequences are also particularly interesting due to the large potential for biological sensors.[15-18]

FF forms multi-level ordered structures, usually into fibrils and tubes, with dimensions ranging from few tens of nanometers up to the micrometer scale. The crystallographic arrangement has been appropriately described according to the hexagonal symmetry group $P6_1$ for self-assembly occurring in an aqueous environment. In this configuration, FF units form cyclic hexamers stacking into a columnar phase parallel to the long axis of the structure with carboxyl and amine groups forming hydrophilic tunnels that host H_2O molecules.[15] Water content within these galleries plays a major role in determining stability, morphology and electronic properties.[19-21]

However, when FF is self-assembled under anhydrous conditions, they are frequently described in terms of orthorhombic groups.[5, 6, 8] Similarly, hydrated FF nanotubes exhibit a hexagonal to orthorhombic phase transition when incubated at temperatures above 140 °C. This phenomenon has been ascribed to the release of water and the change in peptide backbones from a linear conformation to a cyclic one, followed by the reorganization of the crystalline structure in the orthorhombic symmetry group $P22_12_1$.[20] The observed transition is irreversible, and induces strong modifications on L,L,-diphenylalanine micro-/nanostructures (FF-MNSs) properties, ranging from the nanoscopic to the macroscopic level.[6, 8, 22] Clearly, this realignment at the molecular level affects the balance of interactions.

Herein, we report the structure-phase relationship of FF-MNSs in $P6_1$ (called here after Hex) and $P22_12_1$ (Ort) space groups, and their physical-chemical properties towards the modification with poly(allylamine hydrochloride) (PAH) and microperoxidase-11 (MP11). MP11 is an undecapeptide containing a heme-iron group, and is able to exchange electrons with the electrode, offering an excellent electrochemical probe to study the direct electron transfer of the obtained hybrid materials to the electrode.[23, 24] Since the self-assembled network of the FF-MNSs acts as protein-like structures and heme-peptide as the active site, we recreate the stabilization favored by the protein structure using a peptide-based biomaterial. Moreover, we show that the crystal structure influences the conductivity of the scaffold, where the orthorhombic structure is p-type doped by PAH. The developed scaffold was further used for the development of a glucose biosensor, coupling the glucose oxidation promoted by Glucose Oxidase with the peroxide reduction of MP11 supported in the orthorhombic FF-MNSs. The use of the proposed material opens up several applications, not only in biosensing, but also

a. Centro de Ciências Naturais e Humanas, Universidade Federal do ABC, 09210-580, Santo André, SP, Brazil
b. Instituto de Ciências Exatas, Faculdade de Física, Universidade Federal do Sul e Sudeste do Pará, Campus Marabá, 68505-080, Marabá, Pará, Brazil
c. Instituto de Física Teórica, Universidade Estadual Paulista – UNESP, São Paulo, SP, Brazil
d. Department of Physics of Astronomy, University of Missouri, Columbia, Missouri 65211, United States
*Corresponding Author: wendel.alves@ufabc.edu.br
Electronic Supplementary Information (ESI) available: XRD refinement and Raman fitting data are available. See DOI: 10.1039/x0xx00000x

ARTICLE

in semiconductor bioelectronics, supported biocatalysts, and others technological applications.

2 Experimental and Theoretical Methods

Chemicals: K_2HPO_4, KH_2PO_4, H_2O_2 solution 30% (w/w) and KCl were purchased from Synth (Brazil), L,L-diphenylalanine (FF), microperoxidase 11 (MP11), poly(allylamine hydrochloride) (PAH), $K_3[Fe(CN)_6]$, Glucose Oxidase from *Aspergillus Niger*, Nafion (5%) and 1,1,1,3,3,3-hexafluoro-2-propanol (HFIP) were purchased from Sigma-Aldrich (USA). All chemicals were used without any further purification. All solutions were prepared using ultrapure water from a MilliQ® system (resistivity > 18 MΩ cm^{-1}).

Preparation of FF-MNSs in Hexagonal and Orthorhombic structure: The FF-MNSs were prepared by dissolving the lyophilized form of the peptide FF in HFP at a concentration of 100 mg mL^{-1}, and diluting it to 5 mg mL^{-1} with ultrapure water, after the dilution the self-assembly process occurs spontaneously.[1, 25] After 12 hours of aggregation, the diluted mixture was centrifuged for 15 min in a MPW centrifuge at 12000 rpm. The supernatant was removed, and the materials were dried under vacuum overnight, or until complete dryness. At that point, the structures have the hexagonal $P6_1$ crystal structure. To achieve the phase transition the obtained powder was heated to 150°C, kept at this temperature for 60 min, and slowly cooled to RT.[20, 26] After that, the FF-MNSs are in the orthorhombic $P22_12_1$ crystal structure. Those two materials are called Hex and Ort, for the $P6_1$ and $P22_12_1$ structures of FF-MNSs respectively.

Modification of the FF-MNSs with MP11+PAH, and preparation of GC electrodes: First, a stock solution of MP11 in phosphate buffer solution (0.1 mol L^{-1}, pH 7.3) was prepared using 6 mg mL^{-1}, and a stock solution of PAH (0.5 mg mL^{-1}) with pH adjusted to 7 with 0.1 mol L^{-1} HCl solution. To 3 mg of FF-MNSs, 100 µL of the MP11 solution was added, and the volume was adjusted to 0.5 mL with the PAH solution. This dispersion was left shaking for 12 hours at 4°C. All MP11 was adsorbed onto the FF-MNSs matrix since the supernatant solution was colorless. Those dispersions were then used to modify a glassy carbon electrodes (GC) surface.

The GC electrode (0.07 cm^2) was carefully polished with 0.5, 0.03 and 0.01 µm alumina and sonicated in ethanol and water for 10 min each. The modified GC electrode was prepared by depositing a drop (4.5 µL) of the previously described mixture directly on top of the electrode. The solvent was allowed to evaporate at room temperature, and the electrode was used after that.

For detection of glucose with MP11, the modification of the (Ort+MP11+PAH)/GC scaffold was followed by dropping 4.5 µL of Glucose Oxidase (GOx, 12 mg mL^{-1} in PBS). This was then left to dry, after which a 4.5 µL of Nafion (0.5% in PBS) was deposited and again left to dry, covering the whole surface with Nafion polymer.

X-ray diffraction and electron microscopy: X-ray diffraction (XRD) patterns of powdered samples were recorded at room temperature on a Stadi-P (Stoe, Darmstadt, Germany)

diffractometer (transmission configuration). The beam was provided by a Cu-target source, providing monochromatic X-ray photons of λ =0.154056 nm, operating at 40 kV/40 mA. The same amount of the solution used to modify the electrodes was placed on a mica foil, which was spun during data acquisition. A Mythen 1K silicon strip detector was used for data collection. The 2θ range was scanned between 4° and 40°. Scanning electron microscope (SEM) images were obtained using a JEOL FEG-SEM JSM 6330 F microscope at the Laboratory of Electron Microscopy of the Nanotechnology National Laboratory (LNNano), Campinas, Brazil. The materials were deposited in glassy carbon electrodes (0.07 cm^2) used for SEM studies; the films were made as described previously. All films received a thin layer of gold prior to image collection.

FTIR, Raman Spectroscopy and Zeta Potential Measurements: The FTIR spectra of the films were recorded on a Varian spectrometer, model 660-IR, with an attenuated total reflectance device (ATR Pyke). The Raman measurements were performed in a triple spectrometer (T64000, HORIBA Jobin-Yvon) with a thermoelectrically cooled CCD detector (Synapse, HORIBA Jobin-Yvon). The 532 nm line of an optically pumped semiconductor laser (Verdi G5, Coherent) was used as excitation source. The laser power at the sample was maintained at 5 mW, and 50X lenses were used. The zeta potential of the samples were obtained using a Zetasizer NanoZS from Malvern Instruments.

Electrochemical Measurements: Cyclic voltammetry, chronoamperometry and electrochemical impedance spectroscopy were performed using a Potentiostat/ Galvanostat µAutolab Fra 2, Type III. An electrochemical cell containing 10.0 mL of the electrolyte solution was used for all measurements, with a saturated calomel electrode (SCE) as reference, a Pt wire as the auxiliary electrode, and the modified GC electrode as the working electrode. The electrolytes used were phosphate buffer solution 0.1 mol L^{-1} pH 7.3 or 5 mmol L^{-1} $[Fe(CN)_6]^{3-/4-}$ with 0.1 mol L^{-1} KCl solution in phosphate buffer solution 0.1 mol L^{-1} pH 7.3, depending of the experiment. The cathodic catalytic current were measured at +50 mV *vs* SCE, in a nitrogen saturated phosphate buffer solution 0.1 mol L^{-1} pH 7.3, with addition of 10 µmol L^{-1} of H_2O_2 solution. After the background stabilization, the current value was collected; the data is normalized using the apparent electroactive area obtained from the Randles Sevcik Equation. The glucose sensing was performed using the same potential, and electrolytic solution, but in an oxygen saturated solution with additions of 100 µmol L^{-1} of glucose, the data was normalized using the geometric area of the GC electrode and obtained in triplicate.

The EIS experiments were performed in the frequency range of 10^5 to 10^{-1} Hz, with the same solution used to obtain the electroactive area, 5 mmol L^{-1} $[Fe(CN)_6]^{-3/-4}$ and 0.1 mol L^{-1} of KCl in phosphate buffer solution 0.1 mol L^{-1} pH 7.3, at the potential of 0.25 V *vs* SCE. The data were fitted using the Randles circuit by EISSA1 software.[27]

Theoretical Simulations: All the calculations were performed using the density functional theory tight binding (DFTB3)[28] as implemented on the DFTB+ program[29] method as it provides a

good balance between accuracy and efficiency.[21, 30, 31] Here the 3OB-3-1 Slater–Koster parameter set was used.[32, 33]

We first considered a hexagonal nanotube consisting of a packed structure formed by rings of six FF molecules as shown in Fig. 4a. For the orthorhombic structure, we considered an arrangement of cyclic FF structures. All the structures were then relaxed using the conjugate gradient (CG) method with an atomic force tolerance of 0.01 eV/Ang. In all cases, the Brillouin zone was sampled using a Monkhorst-Pack[34] scheme with a 3 x 3 x 3 for the hexagonal and orthorhombic supercell. For the density of states, that sampling was increased threefold in each direction. We then created a surface on each structure and adsorbed the PAH. The supercells were chosen in such a way that the PAH forms a periodic one-dimensional chain on top of the FF-NMs ((2 x 1 x 2) and (2 x 1 x 1) supercells for hexagonal and orthorhombic, respectively). The system was then relaxed again using a k-point sampling of 3 x 1 x 3 and 1 x 3 x 3 for the hexagonal and orthorhombic supercells, respectively.

3 Results and Discussion

Morphological Characterization

The films formed by the modified materials were studied by SEM (Figure 1), and confirmed the presence of the FF-MNSs on it. For both electrodes, a homogeneous dispersion of FF-MNSs on the surface of the electrode is observed. However, the morphology of the two FF-MNSs with MP11 and PAH are different. In (Hex+MP11+PAH), Figure 1A, the hexagonal FF-MNSs network seems to be covered by a PAH layer, forming two layers, one of the FF-MNSs and other of PAH. The SEM images allude to the fact that the interaction of the micro-nanostructures with different materials are distinct. In (Ort+MP11+PAH) film, Figure 1B, the individual orthorhombic FF-MNSs are apparently covered by positively charged PAH, while this coverage is not effective for the hexagonal structure. The interaction between the FF-MNSs and PAH increases the diameter of the structures due to aggregation effects, from ca 2-3 μm (hexagonal) to ca 5 μm (orthorhombic).Both materials were also studied by zeta potential to evaluate the signal and the intensity of the charges present on the surface of the FF-MNSs.

For the hexagonal structure, the obtained zeta potential was -13.1 ±2.5 mV, while for the orthorhombic the value was -45 ±2.5 mV. The more negative zeta potential of the orthorhombic structure is related to a more negatively charged surface, which produces a stronger interaction with the positively-charged PAH polymer. A similar result was observed for the orthorhombic structure modified with the conductive polyaniline forming a core-shell hybrid material.[35, 36]

Spectroscopic Characterization

To characterize the structures at the crystallographic level, we have performed powder diffraction experiments. The results confirmed that the hexagonal phase is indeed $P6_1$, and the orthorhombic is $P22_12_1$,[8, 20] as shown in Figure 2A. By
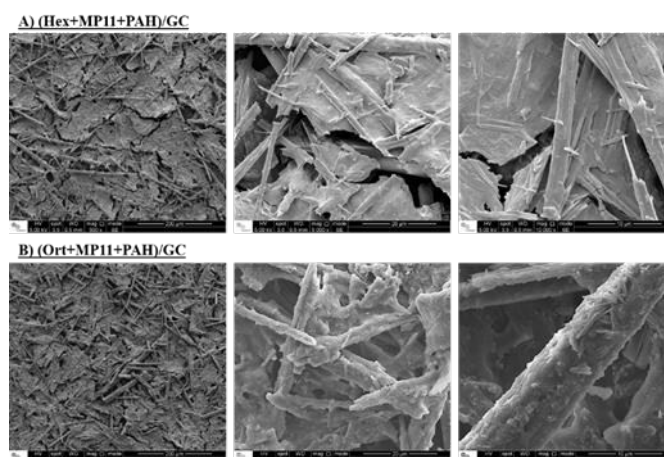

Figure 1. SEM images at different scales of the films on top of glassy carbon electrodes. (A) (Hex+MP11+PAH)/GC, and (B) (Ort+MP11+PAH)/GC. The images were obtained with the same condition as used for electrochemical experiments.

means of Rietveld refinements (Figure S1-S4, presented as Supporting Information material),[37, 38] the presence of MP11 was clearly evidenced and the main characteristic peaks – found in both phases – are indicated by arrows in Figure 2A.

In Figure 2B, the Raman spectra of pristine MP11, Ort/Hex FF-MNSs, and (FF-MNS+MP11+PAH) films, using the 532.8 nm laser excitation are shown. The 1002 cm^{-1} Raman peak is the strongest in FF-MNSs, which arises from a ring deformation mode of the aromatic group. For the pure MP11 film, the principal bands are those around 1600 and 1350 cm^{-1}, which are characteristics of the porphyrin ring vibrational modes. Their intensity may be enhanced by tuning the laser wavelength.[39] Those two regions of the spectrum were fit by Lorentzian functions using OriginPro 9.1 (material presented in supplementary information, Figure S5). The bands at 1642, 1590, 1565 and 1542 cm^{-1} correspond to the C-C bonds vibrational modes of the porphyrin ring. The bands at 1320, 1374 and 1407 cm^{-1} are characteristic vibrations for the C-N bonds of the porphyrin ring, which are sensitive to changes in the oxidation state of the iron atom and π-back-bonding.[40, 41] In Table 1 is shown the relation between the observed Raman shift and the characteristics vibrational modes.

Table 1. Vibrational mode and respective Raman shift (in cm^{-1}) obtained from the results showed in Figure 2B.

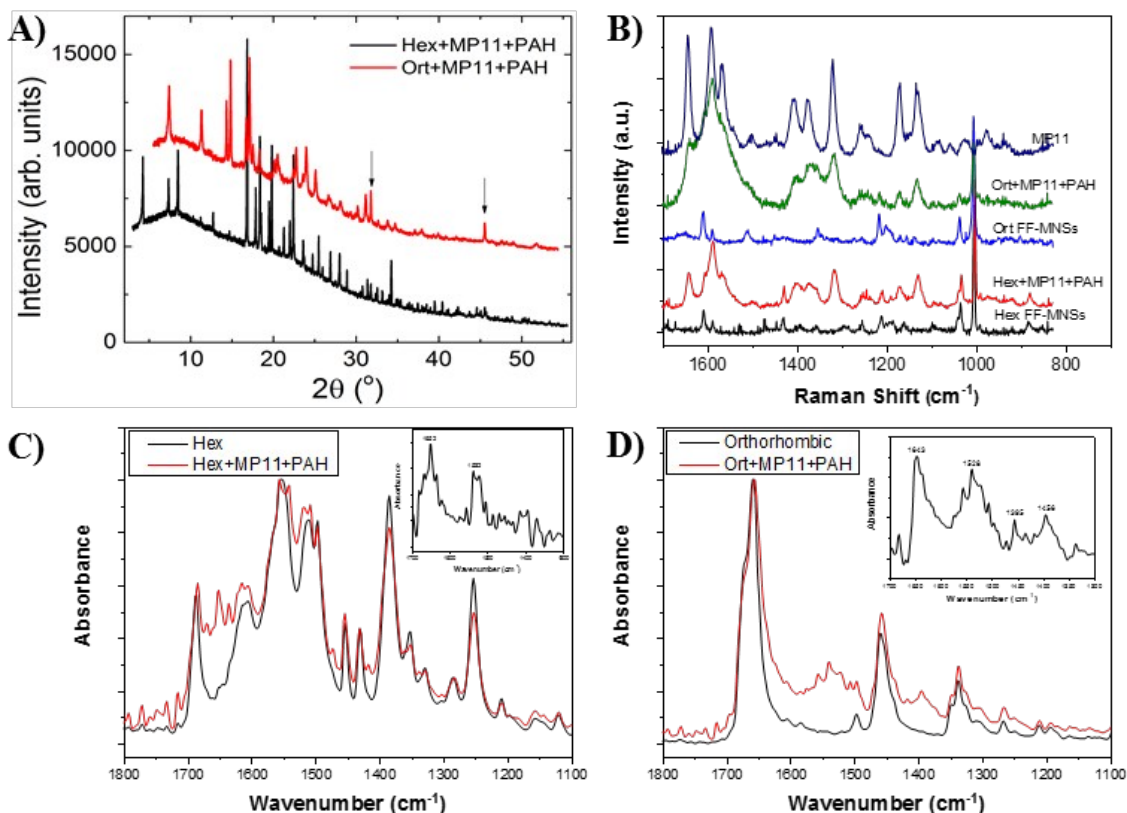| Vibrational Mode	MP11	Hex	Hex+MP11	Ort	Ort+MP11
MP11 δC$_m$H (A$_{2g}$)	1320	-	1315	-	1317
FF ring	-	1356	1356	1352	1351
MP11 C$_a$N (A$_{1g}$)	1374	-	1371	-	1371
MP11 C$_a$N (A$_{2g}$)	1406	-	1400	-	1402
MP11 C$_b$C$_b$ (B$_{1g}$)	1542	-	1545	-	1537
MP11 C$_b$C$_b$ (A$_{1g}$)	1565	-	1563	-	1562
MP11 C$_b$C$_b$ (E$_u$)	1590	-	1587	-	1589
FF ring	-	1587	1587	1587	1586
FF ring	-	1607	1604	1608	1611
MP11 C$_a$C$_m$ (B$_{1g}$)	1642	-	1639	-	1637

Figure 2. Physical chemistry characterization results. A) XRD data obtained for the studied material showing the hexagonal and orthorhombic contribution. B) Raman spectra of the studied materials. The experiments were performed using a 50X magnification lens, and a 532.8 nm laser. C) FTIR spectra of the pure hexagonal and modified hexagonal FF-MNSs films. In the inset is shown the subtracted spectrum of the pure hexagonal spectral contribution from the modified hexagonal material spectrum. D) FTIR spectra of the pure orthorhombic and modified orthorhombic FF-MNSs films. The inset shows the subtracted spectrum of the pure orthorhombic spectral contribution from the modified orthorhombic material spectrum. The insets give information about the MP11 configuration of the two materials.

Both the Hex and the Ort materials with MP11 show slight shifts in the Raman peak positions compared to pristine MP11 Raman frequencies, indicating that there is an interaction between FF-MNSs and MP11. The frequencies show a larger shift for the Ort FF-MNSs sample. For the (Hex+MP11+PAH), the FF-MNSs peak is at 1605 cm^{-1}, which was at 1607 cm^{-1} prior to modification. In the second region the peaks shift to 1315, 1371 and 1400 cm^{-1} showing that the porphyrin ring π^* orbitals are interacting with the FF-MNSs.

A similar result was observed for the (Ort+MP11+PAH), as the Raman peaks in the 1500 cm^{-1} region shifts towards lower frequencies. The MP11 Raman peaks become much broader when intercalated with the orthorhombic FF-MNs as seen in Figure 2B. The full width at half maximum (FWHM) of the Lorentzian peaks are twice as broad when compared to the free MP11 and to (Hex+MP11+PAH), which is an indication of a stronger interaction of MP11 with the orthorhombic FF-MNSs compared to hexagonal. This is most likely due to the disaggregation of MP11 promoted by the hydrophobic surface of the structures.[42] The FWHM of the Raman peaks are presented in Table S1. In general, broadening of the Raman peaks may also signal a decrease in crystallinity. However, the XRD data shows similar peak widths for the two samples. This indicates that the changes in the Raman spectra reflect a strong interaction between MP11 and Ort FF-MNSs.

The Ort FF-MNSs vibrations shift from 1607 to 1611 cm^{-1}. In the second region, peaks at 1317, 1371 and 1402 cm^{-1} are observed. These values are comparable to the Hex case, but the intensity ratios of 1402 to 1371 cm^{-1} peaks were reduced to 0.6 from values close to 1.0 before. These vibrations are related to the C_aN vibrations, and the decrease in the intensity is due to the interaction between the π^* orbitals of the porphyrin ring with the external orbitals of the FF-MNSs, showing a better interaction of MP11 with the Ort structure, as compared to the Hex structure.

The FTIR spectra of the pure FF-MNSs are similar to those previously shown in the literature, especially the amide I band at 1659 cm^{-1} for the Ort FF-MNSs, and the set of bands around 1700 and 1500 cm^{-1} for the amide I and II bands of the Hex FF-MNSs, shown in Figure 2C and 2D respectively.[36] Modification with MP11 and PAH result in some small differences, more noticeably for the orthorhombic material (Figure 2D). A shoulder at 1640 cm^{-1}, and new bands around 1550 and 1400 cm^{-1} are observed. The shift of the amide band I to 1655 cm^{-1} indicates a decrease in the interaction between the amide groups of FF. A better way to observe the difference in the MP11 vibrations is to subtract the unmodified material spectrum from the modified FF-MNSs spectrum. These results are shown in the insets of Figure 2C and 2D. For the (Hex+MP11+PAH) sample, the MP11 amide bands I and II are at

1652 and 1532 cm^{-1}, respectively. Those bands are located at the expected positions for the α-helical structure of the MP11 peptide backbone.[43] For (Ort+MP11+PAH) three intense bands at 1643, 1528 and 1395 cm^{-1} are observed. Again, these bands agree with the α-helical structure of the peptide backbone of the MP11. Additionally, the appearance of the amide III band at 1395 cm^{-1} is a good indication of the high α-helix content in the material (inset in Figure 2D).

The spectroscopy results point towards the interaction of MP11 and FF-MNSs being stronger for the orthorhombic structure, possibly due to the higher hydrophobicity of FF-MNSs when it is in the orthorhombic phase.[42, 44] One would thus expect the latter structure to have a better response in the electrochemical response and sensing application. In the next section, we show that the electrochemical experimental results corroborate the spectroscopy ones.

Electrochemical Characterization and Band-Structure

The electrochemical characterization was performed in a common three-electrode cell. Initially, the apparent electroactive area was studied using [Fe(CN)$_6$]$^{3-/4-}$ as electrochemical probe. The electroactive area of the electrode is proportional to the current, according to the Randles-Sevcik equation,

$$i_p = 268600 n^{\frac{3}{2}} D^{\frac{1}{2}} C v^{\frac{1}{2}} A \ (1)$$

where n is the number of electrons transferred (n=1, in this case), D is the diffusion coefficient of the electroactive species (7.20 x 10^{-6} cm^2 s^{-1}), C is the concentration of the electroactive species (5 x 10^{-6} mol cm^{-3}), v is the scan rate used in V s^{-1}, and A is the electroactive area of the electrode in cm^2. We used the angular coefficient from the i$_p$ *vs* $v^{1/2}$ plot to obtain the area over the range of scan rates. The results demonstrate that the electrode modified with the different structures had different electroactive areas as seen in Figure 3A. The hexagonal material with PAH polymer had a larger apparent electrochemical area compared to the orthorhombic one since it displayed a larger current response. In that way, the calculated areas were: A$_{(Hex+PAH)}$ = 0.084 cm^2 and A$_{(Ort+PAH)}$ = 0.051 cm^2. Modifying the structures with MP11 resulted in a decrease of the area for both materials to 0.061 cm^2 for (Hex+MP11+PAH) and 0.036 cm^2 for (Ort+MP11+PAH) - a decrease of almost 30% in the both cases. An explanation for the smaller electroactive area of the orthorhombic FF-MNSs-modified electrode is the presence of residual negative charges of the orthorhombic material. Since the sample has a more negative zeta potential, it may prevent the diffusion of negatively charged ferricyanide molecules, resulting in a smaller current and by consequence a smaller apparent electroactive area. However, the obtained areas for both electrodes are larger than that of the electrode modified by the (MP11+PAH) film, which is 0.024 cm^2. Thus, the FF-MNSs matrix is able to enhance the electroactive area due to the size of the obtained materials, which results in a rougher and more porous surface, enhancing the current response as shown in the cyclic voltammogram.

To study the MP11 redox process we further characterized the materials in phosphate buffer solution 0.1 mol L^{-1} pH 7.3,

Figure 3B. We observed, for both materials, an excellent current density signal, with the reversible redox process centered at -0.33 V *vs* SCE, value close to the one observed in the literature, -0.4 V *vs* SCE.[45] To obtain the amount of MP11 on the films, we used the area under the anodic curve, since it gives the charge of the electrochemical process that can be converted to molecular units using the Faraday constant (98485 C mol^{-1}). The values of the area coverage (Γ) of MP11 were calculated using the apparent electrochemical active area, and the obtained results showed that the (MP11+PAH) film had the largest coverage value of 1.0 x 10^{-9} mol cm^{-2}, since it is a film cast from a MP11 and PAH solution, having the same concentration as the one used to modify the FF-MNSs. For the modified FF-MNSs, the values were 3.0 x 10^{-10} mol cm^{-2} and 5.9 x 10^{-10} mol cm^{-2} for (Hex+MP11+PAH) and (Ort+MP11+PAH), respectively. This shows the orthorhombic material has twice the enzyme content when compared to the hexagonal sample, showing that the peptide structure can control the adsorption of MP11, and that the orthorhombic can adsorb more species as discussed previously during the spectroscopic characterization.

Electrochemical impedance spectroscopy (EIS) experiments were carried out and used to characterize the modification of electrodes surfaces and their properties when submitted to alternating current at fixed potential (see Figure 3C). Significant differences in the impedance spectra were observed during stepwise modification of the electrodes. The high frequency region of the spectrum gives information about the charge transfer resistance and the electrochemical double layer capacitance, while the low frequency region shows the dependence of the impedance with the diffusion of the electroactive species to the electrode surface. The Randles circuit was chosen to fit the obtained impedance data, since it gives a good approximation of the studied electrochemical system. The circuit was modelled by the electrolyte solution resistance (R$_s$), which is in series with an electrical double-layer capacitor (C$_{DL}$). A constant phase element (CPE) was used to fit the data since it can change depending on the surface organization; the impedance of this element is described according to the function $Z_{CPE}(\omega) = 1/(Q(j\omega)^n$, where Q can be approximate to the capacitance of the electrode, ω is the frequency, and n is a fitting value. In parallel to the CPE, there is a charge transfer resistance element (R$_{CT}$), which is characteristic for each film, and a Warburg element (Z$_w$) that fits the diffusion limits of the spectrum. From the Warburg element, the apparent diffusion coefficient (D) is obtained, from the relation:

$$Z_W(\omega) = \frac{1}{A} * \frac{RT}{n^2 F^2 \sqrt{2}} * \frac{1}{C\sqrt{D}} \ (2)$$

where $Z_W(\omega)$ is the impedance value obtained after the fitting, A is the apparent electrochemical active area, R is the gas constant (8.314 J K^{-1} mol^{-1}), T is the temperature (298K), n is the number of electrons involved in the reaction (n = 1), F is
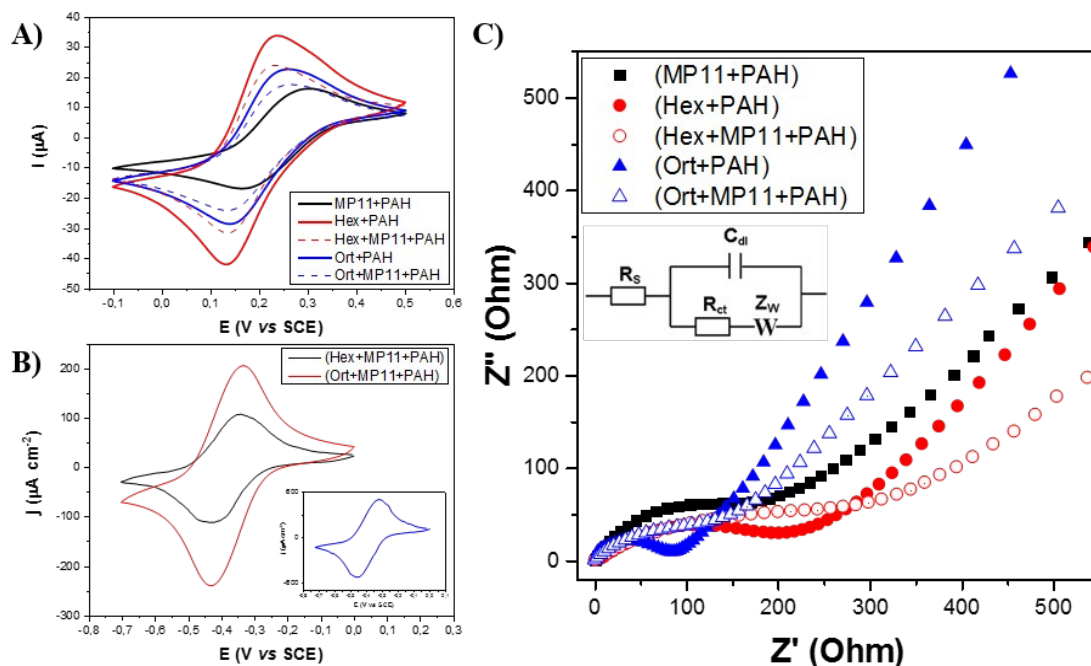
Figure 3. A) Cyclic voltammetry of the obtained films in 5 mmol L^{-1} [Fe(CN)$_6$]$^{-3/-4}$ with 0.1 mol L^{-1} KCl, in 0.1 mol L^{-1} phosphate buffer solution pH 7.3. The scan rate used for the results was 20 mV s^{-1}. B) Cyclic voltammetry of the two modified electrodes in 0.1 mol L^{-1} phosphate buffer solution pH 7.3, scan rate 20 mV s^{-1}. The inset shows the CV for the (MP11+PAH)/GC electrode. C) Nyquist plots of the electrochemical impedance spectroscopy results obtained in the frequency range of 100 kHz to 0.01 Hz with 10 points per decade, applied voltage 0.25 V *vs* SCE, in 5 mmol L^{-1} [Fe(CN)$_6$]$^{-3/-4}$ and 0.1 mol L^{-1} KCl, in 0.1 mol L^{-1} phosphate buffer solution pH 7.3. The electrochemical cell consisted of a Pt wire as CE, SCE as reference and the modified electrodes as WE.

the Faraday's constant, C is the concentration of the electrochemical probe (5 mmol L^{-1}).[46] A schematic representation of the circuit is presented in the inset of Figure 3C. From the obtained fits, the results were compared as a function of parameters. In Table 2, the parameters are listed.

The charge transfer resistance of the assembled layer on glassy carbon (GC) electrodes was 280 and 102 Ω for the (Hex+PAH)/GC and (Ort+PAH)/GC, respectively. When MP11 is added, the R$_{CT}$ value increases to 506 and 142 Ω for the (Hex+MP11+PAH)/GC and (Ort+MP11+PAH)/GC modified electrodes, respectively. The electrode modified with (MP11+PAH), our control sample, had a resistance of 222 Ω, which is significantly different for those observed in the presence of FF-MNSs, suggesting that the orthorhombic FF-MNSs form an electron conductive pathway between the electrode surface and the electrolyte solution when compared to the hexagonal FF-MNSs sample. The presence of MP11 in the modified layer increased the resistance of the film, probably because of its insulating nature and the peptide backbone that could make it harder to conduct electrons

through the film.

The capacitance and diffusion coefficients follows a similar behaviour to the charge transfer resistance. Initially, the films without MP11 had a smaller capacitance, 11.8 and 1.1 µF for the (Hex+PAH) and (Ort+PAH) films, respectively. Thus, adding MP11 in those materials the capacitance increased to 93.6 and 13.2 µF. The control (MP11+PAH) film had a capacitance of 6.2 µF. The obtained values for the films containing FF-MNSs are much larger when compared to the control. For the hexagonal material, the capacitance had a ~15 fold enhancement and for the orthorhombic a factor of ~2. The smaller increase in the capacitance for the orthorhombic material again suggests the formation of an electron transfer pathway through the film, and is even more pronounced in the (Ort+PAH) film that had the smaller capacitance. It shows that the orthorhombic structure facilitates the charge transfer process.

The diffusion of species again showed a similar behaviour, where films containing the orthorhombic material had a faster diffusion, with and without MP11 compared to the films containing the hexagonal MNSs, and with the control. Thus it shows that the orthorhombic material changes the electron transfer pathway of the films. In a previous work published by our group,[20] it was shown that the diffusion coefficients of water molecules on the surface of the structures depends on the structure of the material. On the surface of the orthorhombic structure of FF-MNSs, the coefficients are smaller compared to the hexagonal structure,
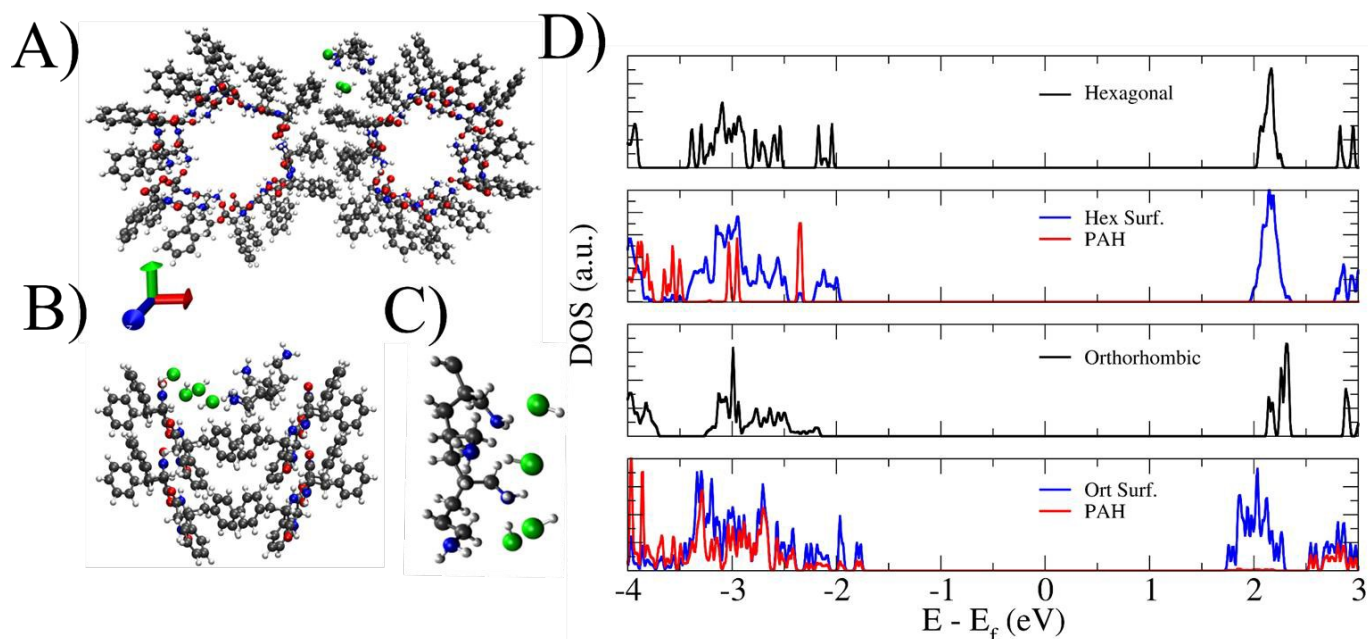
Table 2. Impedance parameters derived from the circuit fit from the data in Figure 3C.

Electrode Configuration	R$_{CT}$(Ω)	Q (µF)	D (10^{-7} cm^2 s^{-1})
(MP11+PAH)/GC	222	6.2	7.5
(Hex+PAH)/GC	280	11.8	2.6
(Hex+MP11+PAH)/GC	506	93.6	7.3
(Ort+PAH)/GC	102	1.1	4.8
(Ort+MP11+PAH)/GC	142	13.2	8.4

Figure 4. Relaxed structures for A) Hexagonal + PAH FF-MNS, and B) Orthorhombic + PAH. C) Two monomers of PAH after relaxation. D) Density of States plot showing the energy of the valence and conduction band of the studied structures. Color code: Grey – C red – O, blue – N, white – H, and green – Cl.

indicating a stronger interaction of the surface with water molecules. As a consequence, the interaction between surrounding molecules and water decreases and the generation of reactive oxygen species depends of those interface properties.[20] In our results, the interpretation is as follows. Since the orthorhombic structures have more MP11, the surface of the MNSs should be more hydrophilic and have more water molecules on that interface, enhancing the diffusion of the electroactive species through the film as it interacts less efficiently with the MNSs. The same behaviour is expected for the unmodified materials, which is what we observe. The (Ort+PAH) film presents a greater diffusion coefficient compared to the (Hex+PAH).

It was surprising that the modification of the materials with MP11 did not give the same response for both phases. While for the hexagonal material, the presence of MP11 enhanced the resistance by about 80% and for the orthorhombic, this enhancement was 40%. Furthermore, the capacitance of the orthorhombic material is the smaller than the hexagonal, and the current flowing to the GC electrode is higher. In order to understand the electronic differences between the two phases of FF-MNS when modified by PAH, electronic structure calculations have been carried out. Previous results estimated the electronic band-gap energies to be 5.6 eV and 6.4 eV for the isolated linear and cyclic diphenylalanine molecules, respectively.[47] For the peptide nanostructures it was experimentally determined to be ~4.0 and ~3.6 eV for the hexagonal and orthorhombic FF-MNSs, respectively.[6] The difference in conductivity cannot be explained only by the band-gap separation as both materials have closed shell electronic structures. There is another competing effect. When the FF-MNSs electrodes are compared to the control electrode (MP11+PAH), the hexagonal phase shows an expected trend of

increased resistance since MP11 is a non-conductive material. Comparing the control *vs* hexagonal, the difference is 286 Ω, and for the orthorhombic, the difference is -80 Ω. It is known in the literature that the orthorhombic structure has semi-conductor properties,[6] and that the orthorhombic phase has a band structure more favourable towards hole transport. The a calculated effective charge transfer integral of the orthorhombic phase equals to 1.1 eV, much higher than the effective electron transport integral of the hexagonal structure 0.3 eV.[47]

To understand the above experimental results, we performed density functional tight binding calculations[28] for the different structures as implemented in the DFTB+ program.[29] The density of states for the bulk calculations in both the Hex and the Ort arrangements are shown in Figure 4. For the hexagonal structure, the band gap is approximately 4.1 eV, whereas for the orthorhombic case it is approximately 4.5 eV. This result is in line with previous calculations[47] showing that the cyclic structure has a larger gap, and consistent with the experimental results.[6] Our results would initially indicate that the Hex arrangement is more conductive than the Ort case. Nevertheless, one notices that the valence band has a larger dispersion in the Ort structure while the conduction band is very narrow for both phases. This means that p-doping the orthorhombic structure could lead to a larger conductance compared to the hexagonal structure.
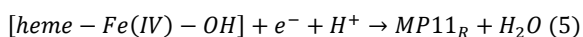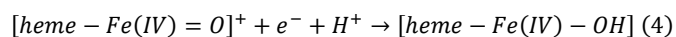
In order to determine whether PAH could lead to such a charge transfer process, we also performed calculations for each phase with PAH adsorbed on the surface of the structure. In the case of Hex+PAH there is small charge transfer from the FF-MNSs to the PAH of approximately 0.03e, whereas for the Ort+PAH that transfer is larger, reaching 0.1e. We notice two important results from this effect: i) the overall gap of the Ort

ARTICLE

structure becomes effectively smaller than the Hex one; while the hexagonal structure has only a small reduction of the gap down to 3.96 eV, the Ort+PAH system has reduction of approximately 1 eV. ii) The second noticeable feature is the presence of PAH states close to the conduction band, a corroboration of the charge transfer process, and an indication that the PAH has a strong interaction with the valence band of the FF-NMS for this phase. In other words, the PAH acts as a p-dopant increasing the conductivity of the orthorhombic phase.

Finally, as shown in previous calculations[21] the presence of water inside the hydrophilic channel of the hexagonal structure leads to a small increase in the dispersion, but it should not significantly alter the conductance trend.

Kinetics analysis of the H_2O_2 reduction

The efficiency of the modified films was tested using the electrocatalytic reduction of hydrogen peroxide in solution. After the background stabilization, the current value was collected. The current is attributed to the electron transfer from the MP11 to the electrode surface. The reaction mechanism follows:

$$[heme - Fe(III)] + H_2O_2 \rightarrow [heme - Fe(IV) = O]^+ + H_2O \ (3)$$

$$[heme - Fe(IV) = O]^+ + e^- + H^+ \rightarrow [heme - Fe(IV) - OH] \ (4)$$

$$[heme - Fe(IV) - OH] + e^- + H^+ \rightarrow MP11_R + H_2O \ (5)$$

where the reaction pathways shows the oxidized forms of MP11, in which oxygen is coordinated to Fe(IV).[48] Equation (3) shows the reaction of H_2O_2 to MP11, and is mainly only controlled by the availability of MP11. However, equations (4) and (5) are influenced by the proton diffusion and the electron transfer from the enzyme to the electrode. From the obtained results shown in Figure 5A, we observed that the current for the orthorhombic modified electrode is much higher than observed for the hexagonal and the pure MP11 film, suggesting that orthorhombic FF-MNSs enhances the catalytic activity of MP11.

The sensitivity of the three modified electrodes was calculated and the obtained values were 12.9 ±0.9 − (MP11+PAH)/GC, 9.7 ±0.7 − (Hex+MP11+PAH)/GC and
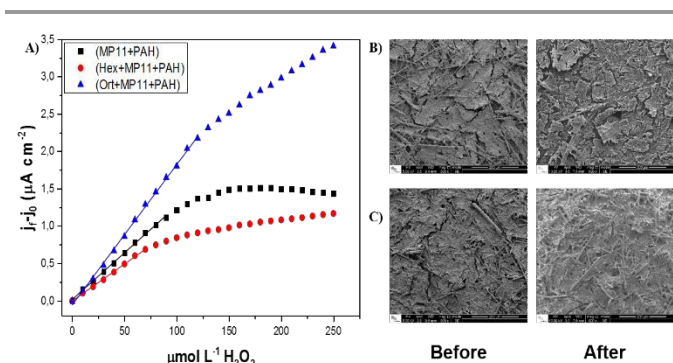

Figure 5. A) Calibration curve for H_2O_2 reduction for the three different modified electrodes with the respective linear fits. The applied potential E= +50 mV *vs* SCE, CE= Pt wire. SEM-FEG images, of the B) (Hex+MP11+PAH)/GC and C) (Ort+MP11+PAH)/GC modified electrodes before and after the H_2O_2 reduction.

18.1 ±0.1 − (Ort+MP11+PAH)/GC nA cm⁻² µmol⁻¹ L. Moreover, these results show that the orthorhombic phase had the largest linear region from 10 to 120 µmol L⁻¹. For the (MP11+PAH) it was 10 to 90 µmol L⁻¹, and for the (Hex+MP11+PAH) it was from 10 to 70 µmol L⁻¹ of H_2O_2. The smaller sensitivity and the linear region of the hex structure may be somewhat surprising initially (Figure 4A) but probing the microstructure of the electrodes gives insights. From SEM images of the electrodes after H_2O_2 reduction we observed that the hexagonal FF-MNSs are not stable after the reaction with H_2O_2 (Figure 5B) while the orthorhombic structure was stable (Figure 5C). The reason for this is still not understood. A possible explanation may be the reaction of the peroxide on the aromatic ring of FF, making it more hydrophilic and thus dissolving it. Another scenario is that since PAH does not cover the FF-MNSs it is more susceptible to dissolution, as seen in some reports where FF-MNSs dissolves in phosphate buffer solution.[8, 49-51]

Following the characterization, the kinetics of the reaction can be described by the equation (6):

$$i = \frac{2F\Gamma}{\frac{1}{k_1 C_S} + \frac{k_2 + k_3}{k_2 k_3 C_H}} \ (6)$$

where i is the current, F is the Faraday constant, Γ is the surface coverage in mol cm⁻², C_S is the concentration of H_2O_2, C_H is the concentration of protons (in this case, around 5.0×10^{-8} mol L⁻¹), and k_1, k_2 and k_3 are the kinetics constants of the reactions of equations (3) to (5). According to equation (6), the higher the amount of MP11 the higher would be the current, and the higher the value of the constants the higher would be the current.

Considering just the first step of the reaction, and since the reaction is kinetically controlled, the electro-catalysis current will be given by:

$$i_1 = 2F\Gamma k_1 C_S \rightarrow \frac{i_1}{C_S 2F\Gamma} = k_1 \ (7)$$

The value of i_1/C_S was found to be the angular coefficient of the linear regression of the j *vs* [H_2O_2] plot. The calculated value for k_1 was 66.8, 77.4 and 160.8 mol⁻¹ L s⁻¹, for the (MP11+PAH), (Hex+MP11+PAH) and (Ort+MP11+PAH), respectively. Those values are comparable to the ones obtained in the literature for carbon nanotubes and graphene modified with MP11, which are 120 and 40 mol⁻¹ L s⁻¹ [48], and 220 mol⁻¹ L s⁻¹ for MP9 absorbed in SnO_2 modified glass.[52] It is observed that the value for the (Hex+MP11+PAH) is about half of the value for the orthorhombic FF-MNSs modified electrode. We believe that the result is closer to the (MP11+PAH) film because of the instability of the hexagonal FF-MNSs.

To obtain the constants for equations 4 and 5, we used the current density value obtained after the saturation of the modified electrode. The current values chosen were the ones for the point at 200 µmol L⁻¹ of H_2O_2. The current density values were 1.5×10^{-6}, 1.1×10^{-6} and 3.0×10^{-6} A cm⁻². The equation used for this step is:

$$i_{23} = 2F\Gamma C_H \left(\frac{k_2 k_3}{k_2 + k_3}\right) \rightarrow \left(\frac{k_2 k_3}{k_2 + k_3}\right) = k_e = \frac{i_{23}}{2F\Gamma C_H} (8)$$

where C_H is the proton concentration in solution (~5×10^{-8} mol L^{-1}). The obtained values for k_e were 1.6×10^5, 1.7×10^5 and 5.3×10^5 mol^{-1} L s^{-1} for the (MP11+PAH), (Hex+MP11+PAH) and (Ort+MP11+PAH) modified electrodes respectively. These values varied around 3.0×10^5 and 4.9×10^5 mol^{-1} L s^{-1} for carbon nanotubes/graphene and graphene modified with MP11, respectively.[48] As mentioned earlier, this part of the reaction involves the electron transfer process from MP11 to the electrode; the higher the value, easier would be the electron transfer process. We note that the smaller values are for (MP11+PAH) and the (Hex+MP11+PAH) modified electrode. We believe that after the reaction, (Hex+MP11+PAH) is similar to the (MP11+PAH) film and hence have similar k_e value. The k_e value for (Ort+MP11+PAH) is 3 times higher than the (Hex+MP11+PAH) mainly due to a higher conductivity.

Our Raman spectroscopy results show an interesting trend. The interaction of the MP11 with the FF-MNSs, changed the position of some bands in the Raman spectra, we here observe preferentially the band corresponding to the $C_a C_m$ (B_{1g}) vibrational mode. It was previously observed that changes in the position of this frequency are directly correlated to the distance between the porphyrin center and pyrrole nitrogen atom. We used the relation $d = -(\Upsilon/K) + \Lambda$, where d is the distance in Å, Υ is the position of the $C_a C_m$ (B_{1g}) vibration in cm^{-1}, K and Λ are two experimental constants, 517.2 Å and 5.16 Å respectively.[41] From the results presented in Table 1, the calculated ring sizes are 1.985, 1.990 and 1.995 Å for the pristine MP11, (Hex+MP11+PAH) and (Ort+MP11+PAH), respectively. From these results, we believe that the MP11 in the orthorhombic FF-MNSs would give a better current response, because the shift in the ring size is accompanied by structural changes in the position of the Fe(III) atom in the porphyrin ring plane; the shorter the distance closer to the plane the Fe atom is. The elongation of the distance changes the reactivity of the MP11, due to shifts in the orbitals energies of the Fe atom, making it more reactive when it is outside the porphyrin ring plane, and turning the hydrogen peroxide electrocatalysis more effective that is the observed response.[53] A similar trend was expected for the (Hex+MP11+PAH) material, however because of structure loss it was more like the (MP11+PAH) sample.

Glucose Biosensor Response

Finally, we explored the role of (Ort+MP11+PAH) as a platform for the development of a coupled biosensor for the detection of glucose. Since hydrogen peroxide is one of the glucose enzymatic oxidation products, it can be used to indirectly quantify the amount of glucose, i.e., coupling the oxidation of glucose with the hydrogen peroxide reduction promoted by the MP11 may be monitored.[54] Our scaffold containing the peptide nanostructures and MP11 act as a wire,
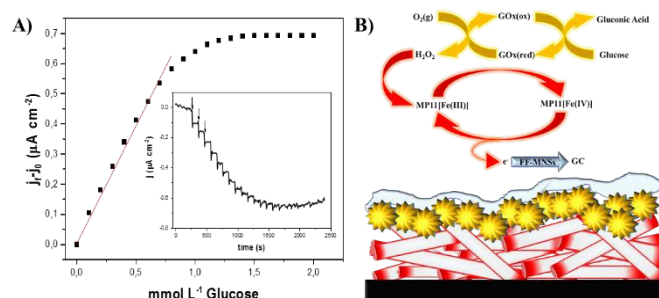

Figure 6. A) Calibration curve of glucose detection for the Nafion/GOx/(Ort+MP11+PAH)/GC electrode with the respective linear fit; the applied potential E= +50 mV *vs.* SCE, counter electrode Pt wire. The inset shows the chronoamperometry data obtained after successive addition of glucose. B) In addition, a scheme representing the reaction pathway through the electrode for the indirect detection of glucose is shown, in the representation, black is the GC electrode, the red rods are the orthorhombic FF-MNSs modified with PAH and MP11, in yellow a representation of GOx, and the pale blue layer corresponds to the Nafion coating.

linking the peroxide reduction that happen on the surface of the materials to the GC surface through a direct electron transfer pathway. The detection was made with successive additions of 100 μmol L^{-1} of glucose in the solution, inset in Figure 6A. We obtained a linear response, Figure 6, for the concentration interval of 100 to 800 μmol L^{-1} in solution with sensitivity of 0.78 ± 0.02 μA cm^{-2} mmol^{-1} L with detection limit of 0.077 μmol L^{-1}. The comparison of our results with previously reported values is shown in the Table 3. The scheme in the Figure 6B shows the possible reaction pathway of the biosensing. Initially glucose is oxidized to gluconic acid due to the reduction of GOx In the presence of molecular oxygen GOx cofactor is regenerated trough the reduction of $O_{2(g)}$ to H_2O_2. The hydrogen peroxide produced can now be reduced by MP11, in the same reaction mechanism described previously (Equation 2-4). The orthorhombic peptide micro-nanostructures act as a molecular wire carrying the electrons produced by that reaction to the glassy carbon electrode, resulting a current signal observed in the chronoamperometry. To our knowledge, this is first report on the use of orthorhombic FF structures in direct biosensing application, which is promising for future development of implantable bioelectronic healthcare devices.

Conclusions

This work demonstrates the importance of crystal structure of self-assembled peptide nanostructures, particularly those based on FF-MNSs, in determining the conductance of networks based on them. The electronic properties of FF-MNSs into an hexagonal and orthorhombic array with monomeric unit of PAH polymer have been theoretically and electrochemically determined. We show for the first time that FF-MNSs organized into an orthorhombic symmetry can be doped with PAH for improvement of hole and electron injection from FF-MNSs, opening opportunities for the development of p-doped self-assembled peptide composite structures. To show the biological applicability of this new approach, we tested the electrocatalytic performance of MP11 embedded in a

Table 3. Comparison of the developed electrode towards different electrode configurations and materials.

Electrode Configuration	Sensitivity	Linear Range	Ref.
(PEI/MP11)$_2$/PEI/(GOx+POPG+DPPG)$_1$/ITO	0.91 µA cm^{-2} mmol^{-1} L	0.113 to 0.565 mmol L^{-1}	[54]
VACNTs/HRP/GOx/GC	89.03 µA mmol L^{-1}	0 to 40 µmol L^{-1}	[55]
AuNPs-SAMs-PNTs/HRP-Gox/GC	0.3 mA mol L^{-1}	0.5 to 2.4 mmol L^{-1}	[56]
GOx-HRP/SBA-15/GC	90 µA cm^{-2} mmol L^{-1}	0.003 to 34 mmol L^{-1}	[57]
(MCM-41/HRP-GOx/Nafion)/GC	467 µA mol L^{-1}	0.05 to 1 mmol L^{-1}	[58]
Nafion/GOx/(MP11+PAH/Ort FF-MNSs)/GC	718 nA cm^{-2} mmol L^{-1}	100 to 800 µmol L^{-1}	This work

Abbreviations: PEI: Poly(ethylene imine); POPG: 1-palmitoyl-2-oleoyl-sn –glycero-3-phosphoglycerol; DPPG: 1,2-dipalmitoyl-phosphatidylglycerol; ITO: Indium tin oxide; VACNTs: vertical aligned carbon nanotubes; HRP: Horseradish peroxidase; AuNPs: gold nanoparticles; SAMs: self-assembled monolayers; PNTs: peptide nanotubes; SBA-15: mesoporous silica; MCM-41: Mobil Composition of Matter 41, mesoporous silica.

FF-MNSs/PAH matrix on the glassy carbon electrodes. The supramolecular peptide nanostructures protect the hemin monomer by preventing degradation and facilitate the catalytic reaction providing porous diffusion channels to allow the transport of substrates to electrode surface. Once again, our results demonstrate that the assembly of FF-MNSs in the orthorhombic phase is essential for improving the direct electron transfer between the immobilized MP11 and the substrate electrode. The as-prepared enzyme electrode presented good direct electrochemistry and electrocatalytic responses to the reduction of H_2O_2. Furthermore, this sensor was then evaluated as mediator for glucose oxidase biosensor. A highly sensitivity (0.78 ±0.02 µA cm^{-2} mmol^{-1} L) with a low detection limit (0.077 µmol L^{-1}) and broad linear detection range up to 800 µmol L^{-1} was achieved. The good sensitivity is related to the presence of a high-dimensional structure based on Ort+MP11+PAH film that can provide an "*electronantennae*" facilitating electron tunnelling between the protein and the electrode. The results suggest that this composite film is a promising material for fabrication of novel multifunctional biosensors for future clinic multimodal diagnosis and therapy.

Acknowledgements

References

1. M. Reches and E. Gazit, *Science*, 2003, **300**, 625-627.
2. X. Yan, P. Zhu and J. Li, *Chem. Soc. Rev.*, 2010, **39**, 1877-1890.
3. L. Adler-Abramovich and E. Gazit, *Chem. Soc. Rev.*, 2014, **43**, 6881-6893.
4. N. Kol, L. Adler-Abramovich, D. Barlam, R. Z. Shneck, E. Gazit and I. Rousso, *Nano Lett.*, 2005, **5**, 1343-1346.
5. J. Ryu and C. B. Park, *Biotechnol. Bioeng.*, 2010, **105**, 221-230.
6. J. S. Lee, I. Yoon, J. Kim, H. Ihee, B. Kim and C. B. Park, *Angew. Chem. Int. Ed.*, 2011, **50**, 1164-1167.
7. A. Kholkin, N. Amdursky, I. Bdikin, E. Gazit and G. Rosenman, *ACS Nano*, 2010, **4**, 610-614.
8. R. C. Bianchi, E. R. Silva, L. H. Dall'Antonia, F. F. Ferreira and W. A. Alves, *Langmuir*, 2014, **30**, 11464-11473.
9. I. O. Matos and W. A. Alves, *ACS Appl. Mater. Interfaces*, 2011, **3**, 4437-4443.
10. J. H. Kim, M. Lee, J. S. Lee and C. B. Park, *Angew. Chem. Int. Ed.*, 2012, **51**, 517-520.
11. T. Cipriano, G. Knotts, A. Laudari, R. C. Bianchi, W. A. Alves and S. Guha, *ACS Appl. Mater. Interfaces*, 2014, **6**, 21408-21415.
12. S. Khanra, T. Cipriano, T. Lam, T. A. White, E. E. Fileti, W. A. Alves and S. Guha, *Adv. Mater. Interfaces*, 2015, **14**, DOI: 10.1002/admi.201500265.
13. Z. Sun, Z. Li, Y. He, R. Shen, L. Deng, M. Yang, Y. Liang and Y. Zhang, *J. Am. Chem. Soc.*, 2013, **135**, 13379-13386.
14. N. Xia, Y. Zhang, K. Chang, X. Gai, Y. Jing, S. Li, L. Liu and G. Qu, *J. Electroanal. Chem.*, 2015, **746**, 68-74.
15. H. Li, Y. Huang, Y. Yu, W. Li, Y. Yin and Genxi Li, *Anal. Chem.*, 2015, **87**, 9251–9256.
16. H. Li, Y. Huang, B. Zhang, X. Pan, X. Zhu and G. Li, *Anal. Chem.*, 2014, **86**, 12138–12142.
17. H. Li, H. Xie, Y. Cao, X. Ding, Y. Yin and G. Li, *Anal. Chem.*, 2013, **85**, 1047–1052.
18. Y. Yu, H. Li, B. Zhang, X. Pan, X. Zhu, Y. Ding and G. Li, *ACS Appl. Mater. Interfaces*, 2015, **7**, 4401–4405.
19. J. Kim, T. H. Han, Y. I. Kim, J. S. Park, J. Choi, D. C. Churchill, S. O. Kim and H. Ihee, *Adv. Mater.*, 2010, **22**, 583-587.
20. M. I. Souza, E. R. Silva, Y. M. Jaques, F. F. Ferreira, E. E. Fileti and W. A. Alves, *J. Pep. Sci.*, 2014, **20**, 554-562.
21. T. Andrade-Filho, F. F. Ferreira, W. A. Alves and A. R. Rocha, *Phys. Chem. Chem. Phys.*, 2013, **15**, 7555-7559.
22. H. Nezammahalleh, G. Amoabediny, F. Kashanian and M. H. Foroughi Moghaddam, *Results Phys.*, 2015, **5**, 11-19.
23. K. S. Prasad, C. Walgama and S. Krishnan, *RSC Adv.*, 2015, **5**, 11845-11849.
24. Q.-L. Zhang, A.-J. Wang, Z.-Y. Meng, Y.-H. Lu, H.-J. Lin and J.-J. Feng, *Microchim. Acta*, 2013, **180**, 581-587.
25. M. Reches and E. Gazit, *Nano Lett.*, 2004, **4**, 581-585.

26. A. Heredia, I. Bdikin, S. Kopyl, E. Mishina, S. Semin, A. Sigov, K. German, V. Bystrov, J. Gracio and A. L. Kholkin, *J. Phys. D Appl. Phys.*, 2010, **43**, 462001.

27. G. A. Ragoisha and A. S. Bondarenko, *Electrochim. Acta*, 2005, **50**, 1553-1563.

28. M. Gaus, Q. Cui and M. Elstner, *J. Chem. Theory Comp.*, 2012, **7**, 931-948.

29. B. Aradi, B. Hourahine and T. Frauenheim, *J. Phys. Chem. A*, 2007, **111**, 5678-5684.

30. J. G. Brandenburg and S. Grimme, *J. Phys. Chem. Lett.*, 2014, **5**, 1785-1789.

31. Y. Zhai and Y. L. Zhao, *J. Theor. Comp. Chem.*, 2013, **12**, 1350019.

32. M. Gaus, A. Goez and M. Elstner, *J. Chem. Theory Comp.*, 2013, **9**, 338-354.

33. M. Kubillus, T. Kubař, M. Gaus, J. Řezáč and M. Elstner, *J. Chem. Theory Comp.*, 2015, **11**, 332-342.

34. H. J. Monkhorst and J. D. Pack, *Phys. Rev. B*, 1976, **13**, 5188-5192.

35. J. Ryu and C. B. Park, *Angew. Chem. Int. Ed.,* 2009, **48**, 4820-4823.

36. H. R. Amaral, S. Kogikoski Jr, E. R. Silva, J. A. Souza and W. A. Alves, *Mater. Chem. Phys.*, 2012, **137**, 628-636.

37. H. Rietveld, *Acta Crystallogr.*, 1967, **22**, 151-152.

38. H. Rietveld, *J. Appl. Crystallogr.*, 1969, **2**, 65-71.

39. T. G. Spiro, J. D. Stong and P. Stein, *J. Am. Chem. Soc.*, 1979, **101**, 2648-2655.

40. Y. P. Myer, R. B. Srivastava, S. Kumar and K. Raghavendra, *J. Protein Chem.*, 1983, **2**, 13-42.

41. S. Choi, T. G. Spiro, K. C. Langry, K. M. Smith, D. L. Budd and G. N. Lamar, *J. Am. Chem. Soc.*, 1982, **104**, 4345-4351.

42. J. S. Lee, J. Ryu and C. B. Park, *Soft Matter*, 2009, **5**, 2717-2720.

43. S. Doerr, U. Schade and P. Hellwig, *Vib. Spec.*, 2008, **47**, 59-65.

44. L. Adler-Abramovich, D. Aronov, P. Beker, M. Yevnin, S. Stempler, L. Buzhansky, G. Rosenman and E. Gazit, *Nat. Nanotechnol.*, 2009, **4**, 849-854.

45. H. M. Marques, *Dalton Trans.*, 2007, 4371-4385.

46. R. N. Vyas, K. Li and B. Wang, *J. Phys. Chem. B*, 2010, **114**, 15818-15824.

47. N. Santhanamoorthi, P. Kolandaivel, L. Adler-Abramovich, E. Gazit, S. Filipek, S. Viswanathan, A. Strzelczyk and V. Renugopalakrishnan, *Adv. Mater. Lett.*, 2011, **2**, 100.

48. K. Komori, T. Terse-Thakoor and A. Mulchandani, *ACS Appl. Mater. Interfaces*, 2015, **7**, 3647-3654.

49. L. Adler-Abramovich, M. Reches, V. L. Sedman, S. Allen, S. J. B. Tendler and E. Gazit, *Langmuir*, 2006, **22**, 1313-1320.

50. V. L. Sedman, L. Adler-Abramovich, S. Allen, E. Gazit and S. J. B. Tendler, *J. Am. Chem. Soc.*, 2006, **128**, 6903-6908.

51. K. B. Andersen, J. Castillo-Leon, M. Hedstrom and W. E. Svendsen, *Nanoscale*, 2011, **3**, 994-998.

52. T. Tatsuma and T. Watanabe, *Anal. Chem.*, 1991, **63**, 1580-1585.

53. J. G. Kleingardner and K. L. Bren, *Acc. Chem. Res.*, 2015, **48**, 1845-1852.

54. J. S. Graça, R. F. de Oliveira, M. L. Moraes and M. Ferreira, *Bioelectrochemistry*, 2014, **96**, 37-42.

55. A. B. Islam, F. S. Tulip, S. K. Islam, T. Rahman and K. C. MacArthur, *IEEE Sens. J.*, 2011, **11**, 2798-2804.

56. B.-W. Park, R. Zheng, K.-A. Ko, B. D. Cameron, D.-Y. Yoon and D.-S. Kim, *Biosens. Bioelectron.*, 2012, **38**, 295-301.

57. Z. Dai, J. Bao, X. Yang and H. Ju, *Biosens. Bioelectron.*, 2008, **23**, 1070-1076.

58. N. Caro-Jara, R. Mundaca-Uribe, C. Zaror-Zaror, J. Carpinelli-Pavisic, M. Aranda-Bustos and C. Peña-Farfal, *Electroanal.*, 2013, **25**, 308-315.